ACS APPLIED MATERIALS & INTERFACES

Forum Article

www.acsami.org

Dependence of the Li-Ion Conductivity and Activation Energies on the Crystal Structure and Ionic Radii in $Li_6MLa_2Ta_2O_{12}$

Wolfgang G. Zeier,*[†] Shiliang Zhou,[†] Beatriz Lopez-Bermudez,[†] Katharine Page,[‡] and Brent C. Melot*[†]

[†]Department of Chemistry, University of Southern California, Los Angeles, California 90089, United States

[‡]Lujan Neutron Scattering Center, Los Alamos National Laboratory, MS H805, Los Alamos, New Mexico 87545, United States

Supporting Information

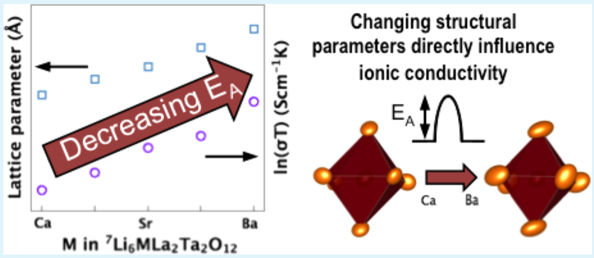

ABSTRACT: Inspired by the promising ionic conductivities of the lithium conducting garnets, we present a comparative study on the influence of the ionic radius of M^{2+} on the 8-coordinate site and the crystal structure on the ionic transport in the solid solution $Li_6MLa_2Ta_2O_{12}$. Neutron diffraction and synchrotron diffraction in combination with AC impedance measurements are employed to understand the systematic substitution with different-sized alkaline earth cations M^{2+}. As may be expected, the unit-cell parameters increase linearly with increasing ionic radius from Ca^{2+} over Sr^{2+} to Ba^{2+}, accompanied by an increase in the polyhedral volumes of the dodecahedral, and tetrahedral positions and the ionic conductivities. While the TaO_6 octahedral volume remain constant, the anisotropic thermal parameters of the coordinating oxygen anions suggest a high degree of rotational freedom with increasing unit-cell size. These structural parameters lead to lower activation energies because of broader Li conduction pathways and a higher flexibility in the crystal lattice, ultimately controlling the ionic conductivities in this class of materials.

KEYWORDS: *solid electrolytes, impedance spectrosopy, neutron diffraction, activation energy, garnets, synchrotron diffraction*

INTRODUCTION

Lithium-ion batteries currently use polymer-based films saturated with organic solvents as electrolytes to achieve the necessary Li^+ mobility for the transport between the cathode and the anode while preventing electrical short-circuits.[1,2] Nevertheless, the electrochemical stability of these electrolytes limits the practical open circuit voltages that can be achieved, and therefore retards the development of higher energy-density batteries.[3] Furthermore, the flammability, toxicity, and potential for leakage associated with the nonaqueous solvents highlights the need for alternative design strategies. The key requirements for a good electrolyte are a high mobility of Li-ions combined with a negligible electronic conductivity while simultaneously being chemically inert toward contact with elemental Li at the anode.[1] Unfortunately, this combination of physical properties is rare. Although high mobility of Li^+ in solid materials has been encountered at elevated temperatures, room-temperature mobility and chemical stability still remains a significant challenge.

Lithium-containing garnets $Li_xM_2M'_3O_{12}$ have recently gained a significant amount of attention as a family of promising solid-state electrolytes due to their exceptionally high ionic conductivity ($\sim 1 \times 10^{-4}$ Scm^{-1}) at room temperature and electrically insulating character.[4,5] This structural family derives from the grossular prototype $Ca_3Al_2Si_3O_{12}$ and contains an open network of $M'O_8$ antiprismatic and MO_6 octahedral polyhedra with a network of tetrahedral sites for Si^{4+} or Li^+ respectively (see Figure 1). The partial occupancy of the interpenetrated tetrahedral and octahedral Li-sites allows facile diffusion of Li ions through the lattice, resulting in a low activation barrier for Li diffusion.[5−8]

A common approach to optimize the performance is to replace M or M′ with an aliovalent cation in order to increase the amount of lithium content in the garnet structure. This type of substitution allows the material to maintain a charge balance while also producing compositions with higher Li content which is known to increase Li-ion conductivities, as typified by $Li_7La_3Zr_2O_{12}$,[9−12] $Li_{3+x}Nd_3Te_{2-x}Sb_xO_{12}$,[13,14] and $Li_5La_3(Ta/Nb)_2O_{12}$.[15−20] As a further example, substitution of La^{3+} with a divalent alkaline earth cation in $Li_5La_3Ta_2O_{12}$ has also been shown to increase the Li content using Ca^{2+},[21] Sr^{2+},[21,22] and Ba^{2+}.[7,22−26] Although this increase in Li content ultimately leads to an enhanced Li-ion conductivity, the difference in the alkaline earth metal is also found to have a significant effect on their ionic conductivities.

In an effort to understand the effects of the size differences of the M^{2+} cation on the ionic transport in this class of materials, the current study focuses on the solid solution $Li_6MLa_2Ta_2O_{12}$, with compositions of M = Ba, $Ba_{0.5}Sr_{0.5}$, Sr, $Sr_{0.5}Ca_{0.5}$ and Ca. Neutron diffraction and synchrotron diffraction studies in combination with AC impedance measurements are employed

Special Issue: New Materials and Approaches for Electrochemical Storage

Received: December 30, 2013
Accepted: March 6, 2014
Published: March 6, 2014

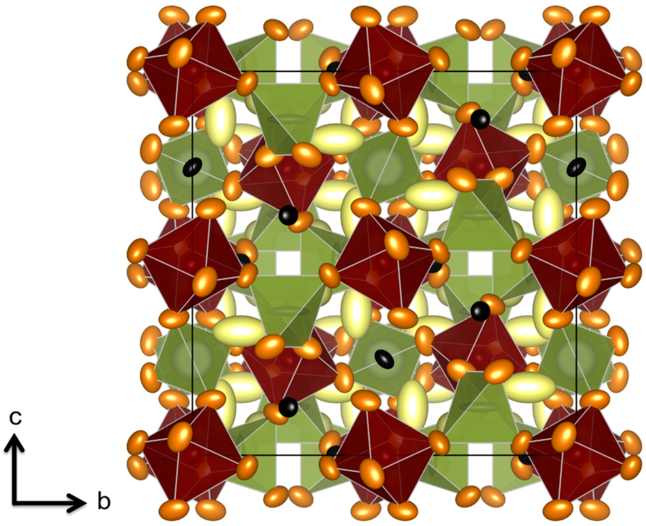

Figure 1. Refined crystal structure of $^{7}Li_6BaLa_2Ta_2O_{12}$ (space group $Ia\bar{3}d$) in polyhedral representation, resulting from time-of-flight neutron scattering data. Ta is shown in dark red in its octahedral coordination, La and M in black and the tetrahedral coordinated ^{7}Li in green. The interstitial Li cation is shown in yellow in its Wyckoff position 48g as ellipsoids according to its refined anisotropic thermal parameters (with 95% probability). These Li^+ cations show a huge degree of anisotropic displacement in their pseudo-octahedral position, probably because of the big cage size, hinting at possible lithium diffusion pathways.

to understand the effect of systematic substitution with different sized alkaline earth cations M^{2+}. The increase in the ionic radius of M^{2+} directly affects the local structure and introduces a certain degree of rotational freedom of the garnet framework, ultimately influencing the ionic transport.

EXPERIMENTAL SECTION

Synthesis. Bulk samples of polycrystalline $Li_6MLa_2Ta_2O_{12}$ with compositions of M = Ba, $Ba_{0.5}Sr_{0.5}$, Sr, $Sr_{0.5}Ca_{0.5}$, and Ca were prepared via solid-state reactions using stoichiometric amounts of Ta_2O_5 (Alfa Aesar, 99%, powder), La_2O_3 (Sigma Aldrich, 99.99%,, powder), LiOH (Sigma Aldrich, ≥ 98%, powder), $Ba(NO_3)_2$ (Sigma Aldrich, ≥99%, powder), $Sr(NO_3)_2$ (Sigma Aldrich, ≥99%, powder) and $CaCO_3$ (Sigma Aldrich, reagent grade plus, powder). La_2O_3 and LiOH were dried at 900 °C for 24 h and 300 °C for 24 h, respectively, and stored under vacuum. For the synthesis of isotopically enriched $^{7}Li_6MLa_2Ta_2O_{12}$, $^{7}LiOH \cdot H_2O$ (Sigma Aldrich, 99.9% ^{7}Li, powder) was used after drying at 300 °C for 48 h to obtain the anhydrous $^{7}LiOH$ as the precursor. For all preparations, a 10 wt % excess of LiOH was added to compensate for the loss of Li at elevated temperatures. The phase purity of the starting materials was verified by standard laboratory X-ray diffraction. The starting materials were thoroughly ground for 30 min in an agate mortar, pressed into pellets using an isostatic press, placed into an alumina crucible. To isolate the pellet from any contact with the alumina crucible, the pellets were covered with the remaining powder of the same composition. The pellets were heated to 973 at 5 K min^{-1} in a box furnace and kept for 6 h to prereact and decompose the precursors. The pellets were subsequently ground thoroughly and pressed into pellets again, using the same sacrificial powder as cover. The materials were then heated to 1173 at 5 K min^{-1} and annealed for 12 h, to obtain phase pure materials. The as-prepared pellets have a theoretical density of ~70%, determined from the mass and geometry of the consolidated discs, and were used for the following electrical characterization. Laboratory X-ray diffraction of consolidated samples do not show any significant texture in this material as expected for these cubic garnet structures. Therefore, properties measured on discs of this polycrystalline material are expected to be isotropic within expected experimental uncertainty and represent a scalar average of the tensor properties.

Physical Characterization. Time-of-flight neutron scattering data were collected at room temperature on polycrystalline powders loaded in a vanadium can using the NPDF instrument at the Lujan Center, Los Alamos Neutron Science Center, Los Alamos National Laboratory. High-resolution synchrotron powder diffraction data were collected using beamline 11-BM at the Advanced Photon Source (APS), Argonne National Laboratory using an average wavelength of 0.413724 Å. Discrete detectors covering an angular range from −6 to 16° 2θ are scanned over a 34° 2θ range, with data points collected every 0.001° 2θ and scan speed of 0.01° s^{-1}. Because of the high X-ray absorption coefficient of the compositions, the powder had been diluted with amorphous SiO_2 prior to the measurements at the synchrotron. The resulting diffraction data were refined using the General Structure Analysis System (GSAS).[27] phase purity of the samples were monitored using standard laboratory X-ray diffraction patterns, collected on a Bruker D8 diffractometer with a CoKα source (λ_1 = 1.78897 Å, λ_2 = 1.79285 Å), equipped with a LynxeEye detector. Scanning electron microscopy (SEM) was performed on a JEOL JSM-7001 microscope (JEOL Ltd.). AC impedance measurements of the pellets (with representative dimensions around 12 mm in diameter and 1 mm in thickness) were performed in air between 18 and 100 °C, using lithium-ion blocking silver electrodes. The silver electrodes were applied with silver paste (SPI Conductive Silver Paste Plus) using a paint thinner to ensure good coverage and thin electrodes and were subsequently cured in air at 800 °C for 10 min. A BioLogic VMP3 potentiostat with an applied 200 mV sinus amplitude in the frequency range of 1 MHz to 500 mHz was utilized to obtain AC impedance data.

RESULTS AND DISCUSSION

Structural Characterization. Although standard laboratory X-ray diffraction has been employed to confirm the phase purity of the different compositions, an accurate and complete structural study cannot be performed using X-rays, due to the very small scattering form factor of Li^+ and the dominance of La^{3+} and Ta^{5+}. Therefore time-of-flight neutron data were collected at room temperature on all compositions of the solid solution, in combination with synchrotron radiation for a better resolution of the lattice parameters and possible impurities. To prevent problems associated with the large absorption cross-section of Li, ^{7}Li enrichment is used because the negative scattering length of ^{7}Li leads to a better contrast compared to the positive scattering length of all other nuclei in $^{7}Li_6MLa_2Ta_2O_{12}$.[5]

Table 1. Resulting Unit-Cell Parameters *a* from the Rietveld Refinement of the Structure of $Li_6MLa_2Ta_2O_{12}$ (space group $Ia\bar{3}d$) against Synchrotron X-ray Powder Diffraction Data from 11-BM (right column) and Time of Flight Neutron Scattering Data from NPDF (left column), with the Respective Reduced χ^2 (goodness of fit)[a]

	NPDF		11-BM	
M	*a* (Å)	χ^2	*a* (Å)	χ^2
Ba	12.99726(7)	3.2	13.011211(8)	2.9
$Ba_{0.5}Sr_{0.5}$	12.91529(4)	2.8	12.92046(2)	1.6
Sr	12.83013(12)	3.1	12.846394(8)	3.8
$Sr_{0.5}Ca_{0.5}$	12.77584(4)	3.4	12.784462(11)	4.3
Ca	12.70877(8)	2.1	12.723830(8)	2.9

[a] Diffraction data were obtained at room temperature.

The space group $Ia\bar{3}d$ and the structural data of $Li_6CaLa_2Ta_2O_{12}$,[21] was used as the initial structural model,

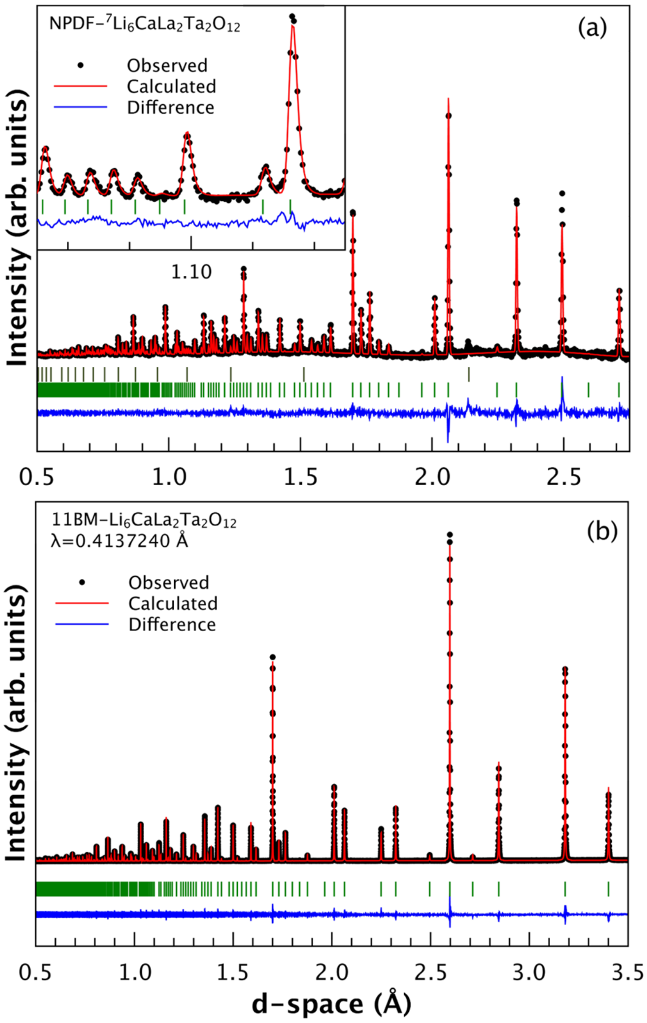

Figure 2. Representative (a) time-of-flight neutron scattering data of $^7Li_6CaLa_2Ta_2O_{12}$ and (b) synchrotron diffraction data of $Li_6CaLa_2Ta_2O_{12}$, including profile fit, profile residuals of the corresponding Rietveld refinement. The secondary reflections (top panel markers) in the neutron diffraction data correspond to the vanadium sample holder. The inset shows the goodness-of-fit at low *d*-spacings. Complete diffraction data of the solid solution $Li_6MLa_2Ta_2O_{12}$ can be found in the Supporting Information.

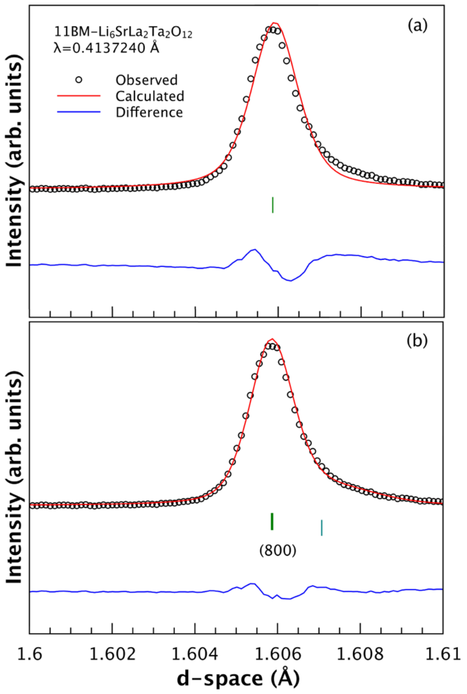

Figure 3. Representative synchrotron diffraction pattern of $Li_6SrLa_2Ta_2O_{12}$ for the (800) reflection including profile fit, profile residuals of the corresponding Rietveld refinement. (a) Fit with only one unit cell and a high degree of asymmetry of the peak at higher *d*-spacing (lower two theta), which cannot be associated with instrumental asymmetry. (b) Fit with a lattice parameter of the main phase and a second phase, which can be associated with continuous spread of nondiscrete lattices in the material, possibly due to an ongoing Li^+/H^+ exchange.

and the input for the various solid solutions were altered accordingly. The thermal parameters and positions of the M^{2+} cations are constrained together with La^{3+} on Wyckoff position 24*c*, because the M cation replaces La on its site. In this structural model, the lithium cations are distributed over the Wyckoff position 24*d* (tetrahedral coordination) and the interstitial pseudo-octahedral position 48*g*.

Neutron diffraction studies by Cussen et al.[6,7] of $Li_5La_3Ta_2O_{12}$ have suggested this structural model may not be accurate and a displacement of the Li^+ occurs, away from 48*g* toward the Wyckoff position 96*h*. However, a refinement of the neutron diffraction data using this structural model with Li^+ on the 48*g* and 96*h* sites does not lead to a good fit, due to some mismatch in the intensity. To improve the refinement, Li^+ in the interstitial position is constrained to the 48*g* site and the anisotropic thermal parameters are refined, to obtain the displacement of Li throughout the whole series of solid solutions. The overall lithium content per unit formula is constraint to a maximum of 6 Li^+, to achieve charge compensation.

For a more accurate determination of the purity and the unit-cell parameters, synchrotron radiation was employed for all compositions in this solid solution and the resulting lattice parameters can be found in Table 1. The diffraction patterns were found to exhibit an asymmetric tail toward the higher *d*-spacings of all reflections (see Figure 3). Instrumental asymmetry was ruled out after the refinement of the 11-BM $Na_2Ca_3Al_2F_{14}$ standard (see the Supporting Information). The best fit is obtained using a second phase with a slightly bigger unit cell, in the cubic garnet space group $Ia\bar{3}d$, in reality representing a continuous spread of nondiscrete lattices in these materials. Figure 3 shows this asymmetry on the reflection of the (800) plane of $Li_6SrLa_2Ta_2O_{12}$, representative for all compositions. We attribute this distribution of unit-cell parameters to the known instability of these lithium conducting garnets in humid atmosphere.[28−32] The resulting Li^+/H^+ exchange is known to lead to an increase in the unit-cell parameters.[31] However, it should be noted that this exchange should lead to the formation of LiOH or $LiCO_3$,[28,30] which has not been found in any of the diffraction patterns. The difference in the lattice parameters of the main phase and the secondary phases are in the range of 0.01 Å and only the lattice parameters of the majority phase are reported in Table 1. A representative refined synchrotron diffraction pattern for $Li_6CaLa_2Ta_2O_{12}$ can be found in Figure 2.

The structural parameters for $^7Li_6BaLa_2Ta_2O_{12}$ and $^7Li_6CaLa_2Ta_2O_{12}$, obtained from the refined time-of-flight

Table 2. Resulting Atomic Positions, Occupancies and Anisotropic Atomic Displacement Parameters from the Refinement of $^{7}Li_6BaLa_2Ta_2O_{12}$ and $^{7}Li_6CaLa_2Ta_2O_{12}$ Time-of-Flight Neutron Scattering Data, For Comparison[a]

	atom	Wyckoff	x	y	z	occupancy
$^{7}Li_6BaLa_2Ta_2O_{12}$ $\chi^2 = 3.2$	Li1	24*d*	0.375	0.0	0.25	0.590(13)
	Li2	48*g*	0.125	0.6770(3)	0.5730(3)	0.705(7)
	Ba	24*c*	0.125	0.0	0.25	0.3333
	La	24*c*	0.125	0.0	0.25	0.6667
	Ta	16*a*	0.0	0.0	0.0	1.0
	O	96*h*	−0.03218(5)	0.04796(6)	0.14233(5)	1.0

atom	Wyckoff	U_{11}	U_{12}	U_{13}	U_{22}	U_{23}	U_{33}
Li1	24*d*	0.004(4)	0.0	0.0	0.066(5)	0.0	0.066(5)
Li2	48*g*	0.116(7)	−0.050(3)	−0.050(3)	0.037(2)	0.007(2)	0.037(2)
Ba	24*c*	0.0153(6)	0.0	0.0	0.0142(3)	0.0053(3)	0.0142(3)
La	24*c*	0.0153(6)	0.0	0.0	0.0142(3)	0.0053(3)	0.0142(3)
Ta	16*a*	0.01295(15)	0.0021(3)	0.0021(3)	0.01295(15)	0.0021(3)	0.01295(15)
O	96*h*	0.0239(4)	0.0072(3)	0.0059(2)	0.0350(4)	0.0038(3)	0.0180(3)

	atom	Wyckoff	x	y	z	occupancy
$^{7}Li_6CaLa_2Ta_2O_{12}$ $\chi^2 = 2.1$	Li1	24*d*	0.375	0.0	0.25	0.546(13)
	Li2	48*g*	0.125	0.6829(2)	0.5671(2)	0.727(6)
	Ca	24*c*	0.125	0.0	0.25	0.3333
	La	24*c*	0.125	0.0	0.25	0.6667
	Ta	16*a*	0.0	0.0	0.0	1.0
	O	96*h*	−0.03112(5)	0.05056(5)	0.14516(5)	1.0

atom	Wyckoff	U_{11}	U_{12}	U_{13}	U_{22}	U_{23}	U_{33}
Li1	24*d*	0.008(4)	0.0	0.0	0.052(4)	0.0	0.052(4)
Li2	48*g*	0.123(6)	−0.037(2)	−0.037(2)	0.020(2)	0.012(2)	0.020(2)
Ca	24*c*	0.0157(6)	0.0	0.0	0.0108(3)	0.00237(3)	0.0108(3)
La	24*c*	0.0157(6)	0.0	0.0	0.0108(3)	0.00237(3)	0.0108(3)
Ta	16*a*	0.0087(2)	0.0003(3)	0.0003(2)	0.0087(2)	0.0003(2)	0.0087(2)
O	96*h*	0.0160(3)	0.0000(2)	−0.0004(2)	0.0173(4)	−0.0015(2)	0.0107(3)

[a] All data sets were obtained at room temperature. Complete diffraction data of the solid solution $Li_6MLa_2Ta_2O_{12}$ can be found in the Supporting Information.

neutron scattering data, are summarized in Table 2 and the resulting structure for the Ba-compound is visualized in Figure 1. A representative diffraction pattern which has been refined for $^{7}Li_6CaLa_2Ta_2O_{12}$ is shown in Figure 2 and the complete structural data can be found in the Supporting Information. Figure 1 shows the crystal structure of $^{7}Li_6BaLa_2Ta_2O_{12}$ including the atoms as ellipsoids according to their refined anisotropic thermal parameters. The Li^+ cations show a huge degree of anisotropic displacement in the pseudo-octahedral Wyckoff position 48*g*, probably because of the big cage size, suggesting possible diffusion pathways for lithium.[11] As reported by Cussen et al.,[6,7] a highly anisotropic displacement can be seen for the Li cations occupying the 48*g* site, which has led to the proposed structural model of Li on the 48*g* and 96*h* interstitial sites. While this may seem contradictory, both structural models and representations depict the Li distribution throughout the structure and the Li-ion pathways. Indeed, the anisotropic thermal parameters of the Ca-containing compound exhibit a lower degree of displacement in their smaller octahedral volume (see Figure 4d), which is in agreement with their smaller ionic radius of M^{2+} and lower ionic conductivities.

The refined lattice parameters (see Table 1) and polyhedral volumes along the series of solid solutions $^{7}Li_6MLa_2Ta_2O_{12}$, with compositions of M = Ba, $Ba_{0.5}Sr_{0.5}$, Sr, $Sr_{0.5}Ca_{0.5}$ and Ca, are shown in Figures 5 and 4, respectively. As expected, the unit-cell parameter *a* increases linearly with the increase in the ionic radius of the M^{2+}-cation from Ca to Ba, clearly following Vegard's law. Because of the increase in the lattice parameter and unit-cell volume, the polyhedral volumes of the dodecahedral $(La/M)O_8$, tetrahedral LiO_4 and pseudo-octahedral LiO_6 sites increase concurrently. Especially the increasing LiO_6 volume leads to an increased cage size for the conducting Li^+ cation, resulting in the above-mentioned displacement. However, the polyhedral volumes of the TaO_6 octahedra remain constant throughout the series, showing the high bond strength of the Ta−O bond compared to all other bonds in these materials. To retain constant TaO_6 volumes through the solid solutions, the coordinates of the oxygen positions need to shift linearly, as is indeed the case (see the Supporting Information).

Although the behavior of the Ta−O bonds is expected, the refined anisotropic thermal parameters of oxygen give insight into an interesting structural change. With increasing unit-cell size from Ca^{2+} to Ba^{2+} the anisotropic thermal parameters of oxygen change significantly, which can be seen in Figure 5 comparing the Ca and Ba compounds. The trend of the increasing anisotropic thermal displacement parameters U_{11}, U_{22} and U_{33} with increasing unit-cell size can be found in the Supporting Information. The oxygen anions in the Ca compound exhibit a very low degree of anisotropy leading to nearly spherical oxygen distribution around their 96*h* Wyckoff position. However, in $^{7}Li_6BaLa_2Ta_2O_{12}$ the anisotropic thermal parameters are big leading to a more ellipsoidal distribution, showing a certain degree of rotational freedom in this structure. The smaller ionic radius of Ca^{2+} leads to a smaller unit cell and

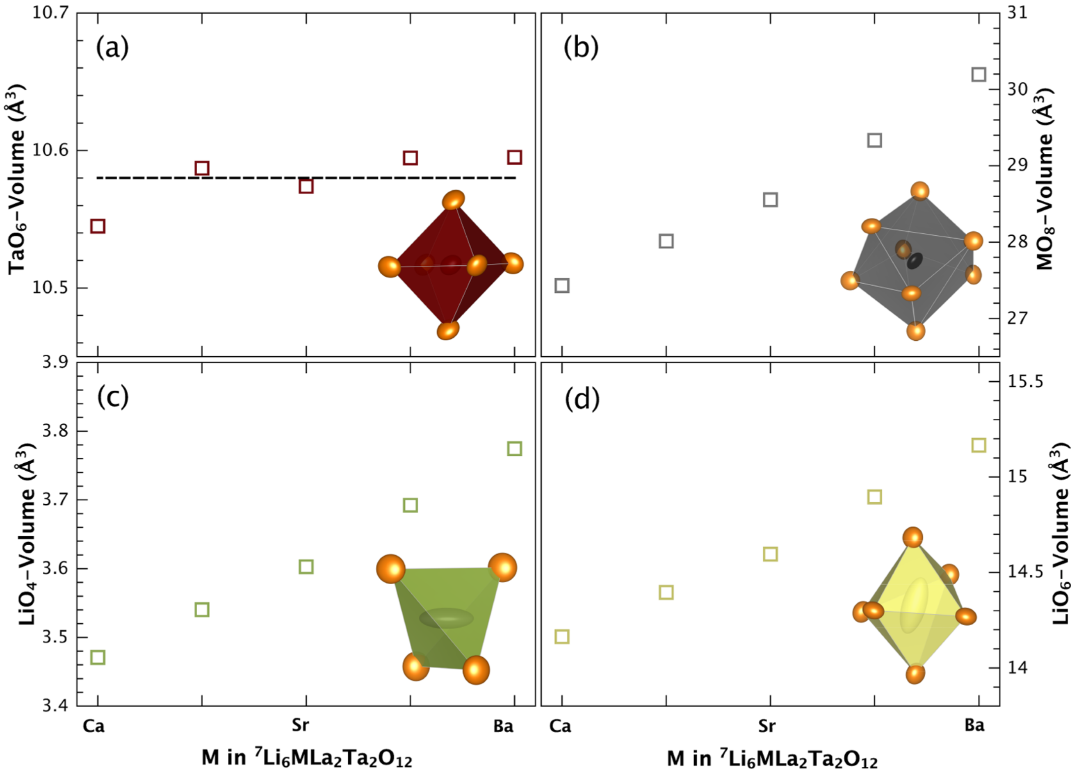

Figure 4. Room-temperature structural data resulting from neutron diffraction studies on $^7Li_6MLa_2Ta_2O_{12}$. Substitution with the earth alkaline cations on the dodecahedral site lead to a linear increase in the (b) dodecahedral $(M/La)O_8$, (c) tetrahedral $^7LiO_4$, and (d) pseudo-octahedral $^7LiO_6$ volumes. (a) TaO_6 octahedral volumes remain constant (within the synthetic uncertainties) throughout the whole series of solid solutions, indicative of the strong bond between tantalum and oxygen.

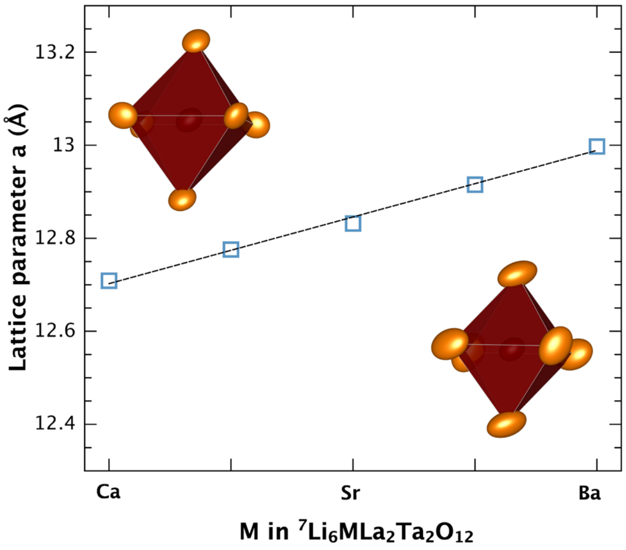

Figure 5. Refined lattice parameters, resulting from neutron diffraction studies on $^7Li_6MLa_2Ta_2O_{12}$. Substitution with the earth alkaline cations on the dodecahedral site lead to a linear increase in the lattice parameters. The two insets depict the refined anisotropic thermal parameters (with 95% probability) of the oxygen in the TaO_6 octahedra for $^7Li_6CaLa_2Ta_2O_{12}$ (left) and $^7Li_6BaLa_2Ta_2O_{12}$ (right). The increasing unit-cell parameters from the increasing ionic radii (Figure 4) lead to a higher degree of rotational freedom in the TaO_6 octahedra.

therefore a more tightly packed lattice, reducing the degree of rotational freedom, which may ultimately affect the Li-diffusion and therefore the ionic conductivity for these materials.

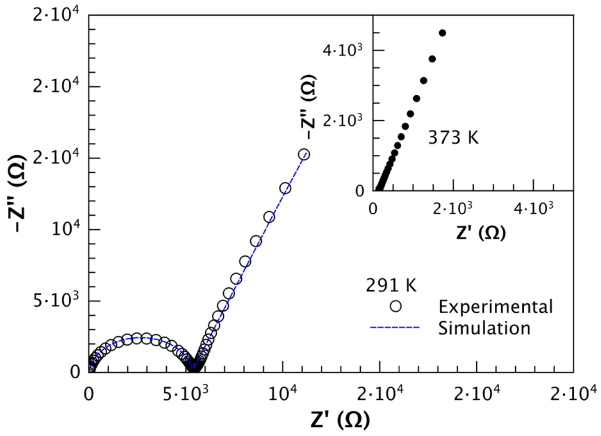

Figure 6. Typical impedance plot obtained for $Li_6BaLa_2Ta_2O_{12}$ at 18 °C in air, using Ag electrodes in the frequency range of 1 MHz to 500 mHz. The appearance of a tail at the low frequency side of the slightly depressed semi circle suggests blocking of the mobile Li ions by the Ag electrode. The inset shows typical impedance data at 373 K. The blue line shows the equivalent circuit fit consisting of a constant phase element (CPE) in series with a parallel CPE/resistor component.

Transport Properties. AC impedance spectroscopy has been employed to assess the influence of the changes in the crystal structure on the ionic transport in $Li_6MLa_2Ta_2O_{12}$. A typical impedance plot of $Li_6BaLa_2Ta_2O_{12}$ at 18 °C and at 100 °C is shown in Figure 6, and the corresponding impedance data for the remaining compositions can be found in the Supporting Information. The appearance of a tail at the low frequency side can be attributed to the Li-ion blocking Ag-electrodes and is

Table 3. Lithium Ionic Conductivities σ of the Solid Solution $Li_6MLa_2Ta_2O_{12}$ with Different M at 291 and 373 K, Respectively[a]

M	σ_{291K} (S cm^{-1})	σ_{373K} (S cm^{-1})	D_{291K} (cm^2 s^{-1})	E_A (eV)
Ba	1.5×10^{-5}	5.6×10^{-4}	2.1×10^{-10}	0.47
$Ba_{0.5}Sr_{0.5}$	7.1×10^{-6}	2.8×10^{-4}	9.9×10^{-11}	0.45
Sr	5.4×10^{-6}	2.1×10^{-4}	7.5×10^{-11}	0.45
$Sr_{0.5}Ca_{0.5}$	3.2×10^{-6}	2.0×10^{-4}	4.3×10^{-11}	0.50
Ca	2.2×10^{-6}	9.4×10^{-5}	2.9×10^{-11}	0.47

[a] The diffusion coefficients D at 291 K have been calculated using the Nernst–Einstein equation for diffusion (eq 1) and the respective activation energies have been extracted from the Arrhenius plots of Figure 7 (eq 2). All ionic conductivities and diffusion coefficients increase with increasing ionic radius and unit-cell size.

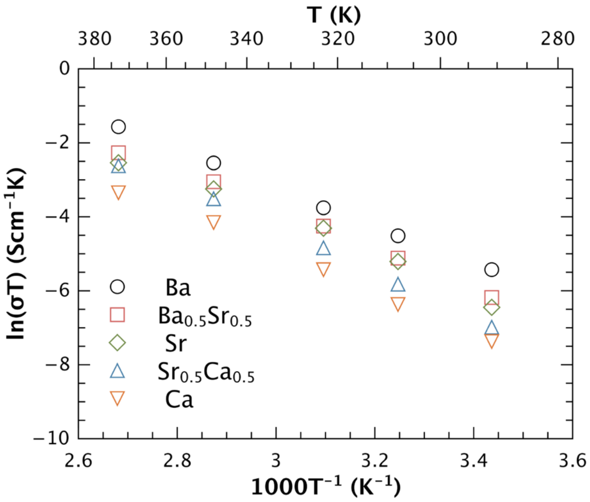

Figure 7. Arrhenius plots for the total lithium ion conductivities of $Li_6MLa_2Ta_2O_{12}$ at different temperatures. With increasing ionic radius of the M cation, the Li-ionic conductivity increases. The respective activation energies can be found in Table 3.

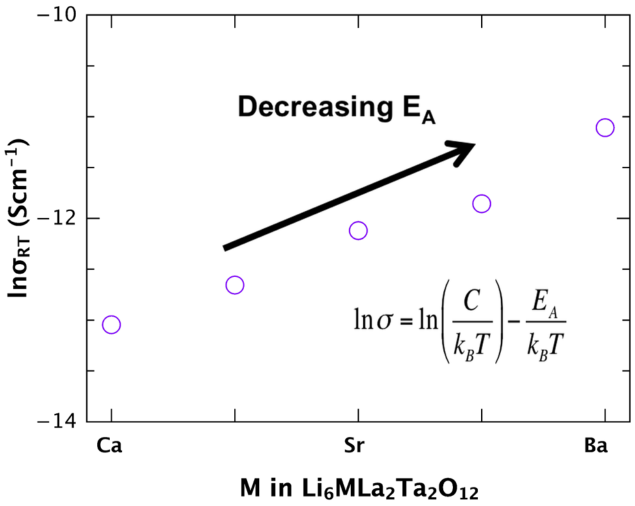

Figure 8. Room-temperature lithium ionic conductivities of different compositions in the solid solution $Li_6MLa_2Ta_2O_{12}$. Assuming a constant pre factor C, due to a constant charge carrier density and very small changes in the Li–Li distance (see the Supporting Information), this increase in ionic conductivities can qualitatively be attributed to a decrease in the activation energies for Li^+ conduction from Ca over Sr to Ba.

indicative of Li-ion diffusion in the bulk sample. A resolution of the grain boundary and bulk contributions cannot be obtained, leading to only one semicircle in the impedance spectra of all samples. Geometrical densities in the measured pellets do not exceed 70% of the theoretical density, and attempts to further consolidate these materials were not successful. This is in accordance with the observations by Awaka et al.,[21] and the poor resolution between the grain and bulk contribution can be attributed to the low density. Scanning electron microscopy micrographs can be found in the Supporting Information, showing the reduced density in these materials. Nevertheless, the grains are well connected, which lead to comparable ionic conductivities as previously observed.[21,22] All semicircles obtained pass through the origin and can therefore be attributed as the bulk properties.[33] The semi circles are slightly depressed, possibly because of different time constants τ resulting from the lower density and small differences in the grain sizes.[33] All impedance data has been fitted using an equivalent circuit consisting of a constant phase element (CPE) in series with a parallel CPE/resistor component. The single constant phase element represents the nonideal diffusion occurring on the Li-blocking Ag-electrodes, resulting in the tail at the low-frequency side.

The Li-ionic conductivities obtained at 18 °C and at 100 °C can be found in Table 3. All values are comparable to the reported data by Thangadurai et al.[22] and Awaka et al.,[21] of σ(Ca, 27 °C = 2.2×10^{-6}, σ(Sr, 22 °C) = 7.0×10^{-6}, and σ(Ba, 25 °C) = 1.3×10^{-5}. An increase in the ionic conductivites can be seen from Ca to Ba. This increase is expected because of the linear increase in the unit-cell parameters and the resulting broader diffusion pathways. The diffusion coefficients D at room temperature (Table 3) have been obtained using the Nernst–Einstein relation[34]

$$\sigma = \frac{q^2 nD}{k_B T} \tag{1}$$

with the elementary charge q ($q = 1.602 \times 10^{-19}$ C), the charge carrier concentration n (i.e., number of Li cations per unit-cell volume), the Boltzmann constant k_B, and the temperature T. The calculated diffusion coefficients increase with increasing unit-cell size and are in good agreement with the diffusion coefficients in this class of materials, obtained through spectroscopical and electrical methods.[16,35]

Temperature-dependent ionic conductivities of all compositions of $Li_6MLa_2Ta_2O_{12}$ are shown in Figure 7 between 18 and 100 °C. Reproducible electrical impedance data in air could not be obtained at higher temperatures, due to a degree of history and a kink in the data upon cooling after the pellets were heated to temperatures above 100 °C. This behavior might be attributed to the above-mentioned Li^+/H^+ exchange. The measured ionic conductivities can be used to obtain the activation energies of the Li-ion conduction, using the Arrhenius equation[34]

$$\sigma = \frac{C}{k_B T}\exp\left(-\frac{E_A}{k_B T}\right) \tag{2}$$

where E_A is the activation energy of ion motion, C the pre(-exponential factor) and T the temperature. The pre factor C is dependent on the density of interstitial ions in interstitial diffusion and the unit jump distance of the ion. Obtained activation energies of the whole series of solid solutions are given in Table 3, and are all between 0.4 and 0.5 eV as previously reported for these materials.[21−23,25]

Although a tighter packed lattice and smaller lattice parameters lead to lower ionic conductivities as expected, this trend is not apparent in the calculated activation energies. Because of the above-mentioned Li^+/H^+ exchange, these materials are not entirely phase pure and show a certain degree of temperature instability. This will ultimately lead to small errors in the extraction of the activation energies from the temperature dependent ionic conductivites, therefore hiding any real trends.

However, the increase in the ionic conductivity may ultimately be connected to a decrease in the activation energies. Whereas the Li-content and therefore the charge carrier density remains constant throughout this series, the increase in the lattice parameters, the softer lattice and the bigger anisotropic Li displacement lead to a higher Li-mobility. In order to circumvent the temperature dependence, the room temperature ionic conductivities of the solid solutions $Li_6MLa_2Ta_2O_{12}$ have been plotted against their compositions in Figure 8. The logarithmic of the ionic conductivities at room temperature increase linearly with increasing size of the M^{2+} cation. Assuming similar densities[36,37] and a constant pre factor *C*, because of a constant charge carrier density and very small changes in the Li−Li distance (see the Supporting Information), this increase can be qualitatively attributed to a decrease in the activation energies for Li^+-conduction from Ca over Sr to Ba.

CONCLUSION

In summary, we have shown the effect of the M^{2+} cation size on the structural and ionic transport properties in the solid solution $Li_6MLa_2Ta_2O_{12}$. The increase in the ionic radius of M from Ca over Sr to Ba leads to an increase in the lattice parameters and an increase in the polyhedral volumes of LiO_4 and $(M/La)O_8$. This increasing unit cell results in a less tightly packed lattice and directly affects the local structure and introduces a certain degree of rotational freedom of the TaO_6 octahedra as well as leading to broader diffusion pathways for Li^+ conduction as seen in the composition-dependent anisotropic displacement parameters of Li^+. These changes in the structural properties directly influence the activation energies in this class of materials, ultimately leading to lower ionic conductivities due to a higher flexibility of the crystal lattice and broader diffusion pathways.

ASSOCIATED CONTENT

Supporting Information

Refinements of the neutron time-of-flight and synchrotron diffraction data including the patterns, plots of the oxygen positions, Li1−Li2 distances and the anisotropic thermal parameters U_{11}, U_{22}, and U_{33}. Furthermore, scanning electron micrographs, tables for the refined atomic positions occupancies and anisotropic atomic displacement parameters can be found along with the complete impedance data of all compounds at room temperature and 100 °C. This material is available free of charge via the Internet at http://pubs.acs.org.

AUTHOR INFORMATION

Corresponding Author

*E-mail: zeier@usc.edu; melot@usc.edu.

Notes

The authors declare no competing financial interest.

ACKNOWLEDGMENTS

B.C.M., W.G.Z., and S.Z. gratefully acknowledge financial support through start-up funding provided by the Dana and David Dornsife College of Letters and Sciences at the University of Southern California. W.G.Z. also acknowledges the support by a fellowship within the Postdoc-Program of the German Academic Exchange Service (DAAD). The authors thank Chirranjeevi Balaji Gopal for his help and the discussions while building up the impedance measurement system. This work benefited from the use of the NPDF beamline at the Lujan Center at Los Alamos Neutron Science Center, funded by DoE BES. Los Alamos National Laboratory is operated by Los Alamos National Security LLC under DoE Contract DE-AC52-06NA25396. Use of the Advanced Photon Source at Argonne National Laboratory was supported by the U.S. Department of Energy, Office of Science, Office of Basic Energy Sciences, under Contract DE-AC02-06CH11357.

REFERENCES

(1) Goodenough, J. B.; Park, K.-S. The Li-Ion Rechargeable Battery: A Perspective. *J. Am. Chem. Soc.* **2013**, *135*, 1167−1176.

(2) Tarascon, J.-M.; Armand, M. Issues and Challenges facing Rechargeable Lithium Batteries. *Nature* **2001**, *414*, 359−367.

(3) Shao, Y.; Ding, F.; Xiao, J.; Zhang, J.; Xu, W.; Park, S.; Zhang, J.-G.; Wang, Y.; Liu, J. Making Li-Air Batteries Rechargeable: Material Challenges. *Adv. Funct. Mater.* **2013**, *23*, 987−1004.

(4) Thangadurai, V.; Weppner, W. Recent Progress in Solid Oxide and Lithium Ion Conducting Electrolytes Research. *Ionics* **2006**, *12*, 81−92.

(5) Cussen, E. J. Structure and Ionic Conductivity in Lithium Garnets. *J. Mater. Chem.* **2010**, *20*, 5167−5173.

(6) Cussen, E. J. The Structure of Lithium Garnets: Cation Disorder and Clustering in a New Family of fast Li^+ Conductors. *Chem. Commun.* **2006**, 412−413.

(7) O'Callaghan, M. P.; Cussen, E. J. Lithium Dimer Formation in the Li-Conducting Garnets $Li_{5+x}Ba_xLa_{3-x}Ta_2O_{12}$. *Chem. Commun.* **2007**, *12*, 2048−2050.

(8) Xie, H.; Alonso, J. A.; Li, Y.; Fern, M. T.; Goodenough, J. B. Lithium Distribution in Aluminum-Free Cubic $Li_7La_3Zr_2O_{12}$. *Chem. Mater.* **2011**, *23*, 3587−3589.

(9) Murugan, R.; Thangadurai, V.; Weppner, W. Fast Lithium Ion Conduction in Garnet-type $Li_7La_3Zr_2O_{12}$. *Angew. Chem., Int. Ed.* **2007**, *46*, 7778−8771.

(10) Buschmann, H.; Dölle, J.; Berendts, S.; Kuhn, A.; Bottke, P.; Wilkening, M.; Heitjans, P.; Senyshyn, A.; Ehrenberg, H.; Lotnyk, A.; Duppel, V.; Kienle, L.; Janek, J. Structure and Dynamics of the Fast Lithium Ion Conductor $Li_7La_3Zr2O_{12}$. *Phys. Chem. Chem. Phys.* **2011**, *13*, 19378−19392.

(11) Han, J.; Zhu, J.; Li, Y.; Yu, X.; Wang, S.; Wu, G.; Xie, H.; Vogel, S. C.; Izumi, F.; Momma, K.; Kawamura, Y.; Huang, Y.; Goodenough, J. B.; Zhao, Y. Experimental Visualization of Lithium Conduction Pathways in Garnet-type $Li_7La_3Zr2O_{12}$. *Chem. Commun.* **2012**, *48*, 9840−9842.

(12) Rangasamy, E.; Wolfenstine, J.; Sakamoto, J. The Role of Al and Li Concentration on the Formation of Cubic Garnet Solid Electrolyte of Nominal Composition $Li_7La_3Zr2O_{12}$. *Solid State Ion.* **2012**, *206*, 28−32.

(13) O'Callaghan, M. P.; Powell, A. S.; Titman, J. J.; Chen, G. Z.; Cussen, E. J. Switching on Fast Lithium Ion Conductivity in Garnets: The Structure and Transport Properties of $Li_{3+x}Nd_3Te_{2-x}Sb_xO_{12}$. *Chem. Mater.* **2008**, *15*, 2360−2369.

(14) Cussen, E. J.; Yip, T. W.; O'Neill, G.; O'Callaghan, M. P. A Comparison of the Transport Properties of Lithium-Stuffed Garnets

and the Conventional Phases $Li_3Ln_3Te_2O_{12}$. *J. Solid State Chem.* **2011**, *184*, 470−475.

(15) Thangadurai, V.; Kaack, H.; Weppner, W. Novel Fast Lithium Ion Conduction in Garnet-Type $Li_5La_3M_2O_{12}$ (M = Nb, Ta). *J. Am. Ceram. Soc.* **2003**, *86*, 437.

(16) Truong, L.; Narayanan, S.; Thangadurai, V. Recent Progress in Garnet-Type Structure Solid Li ion Electrolytes: Composition−Structure−Ionic Conductivity Relationship and Chemical Stability Focused. *ECS Trans.* **2013**, *45*, 21−29.

(17) Narayanan, S.; Ramezanipour, F.; Thangadurai, V. Enhancing Li Ion Conductivity of Garnet-Type $Li_5La_3Nb_2O_{12}$ by Y-and Li-Codoping: Synthesis, Structure, Chemical Stability, and Transport Properties. *J. Phys. Chem C* **2012**, *116*, 20154−20162.

(18) Nyman, M.; Alam, T. M.; McIntyre, S. K.; Bleier, G. C.; Ingersoll, D. Alternative Approach to Increasing Li Mobility in Li-La-Nb/Ta Garnet Electrolytes. *Chem. Mater.* **2010**, *22*, 5401−5410.

(19) Gao, Y.; Wang, X.; Wang, W.; Fang, Q. Sol-Gel Synthesis and Electrical Properties of $Li_5La_3Ta_2O_{12}$ Lithium Ionic Conductors. *Solid State Ionics* **2010**, *181*, 33−36.

(20) Mariappan, C. R.; Gnanasekar, K. I.; Jayaraman, V.; Gnanasekaran, T. Lithium Ion Conduction in $Li_5La_3Ta_2O_{12}$ and $Li_7La_3Ta_2O_{13}$ Garnet-type Materials. *J. Electroceram.* **2013**, *30*, 258−265.

(21) Awaka, J.; Kijima, N.; Takahashi, Y.; Hayakawa, H.; Akimoto, J. Synthesis and Crystallographic Studies of Garnet-related Lithium-Ion Conductors $Li_6CaLa_2Ta_2O_{12}$ and $Li_6BaLa_2Ta_2O_{12}$. *Solid State Ionics* **2009**, *180*, 602−606.

(22) Thangadurai, V.; Weppner, W. $Li_6ALa_2Ta_2O_{12}$ (A = Sr, Ba): Novel Garnet-Like Oxides for Fast Lithium Ion Conduction. *Adv. Funct. Mater.* **2005**, *15*, 107−112.

(23) Murugan, R.; Thangadurai, V.; Weppner, W. Lithium Ion Conductivity of $Li_{5+x}Ba_xLa_{3-x}Ta_2O_{12}$ (x?=?0−2) with Garnet-related Structure in Dependence of the Barium Content. *Ionics* **2007**, *13*, 195−203.

(24) Murugan, R.; Thangadurai, V.; Weppner, W. Effect of Lithium Ion Content on the Lithium Ion Conductivity of the Garnet-like Structure $Li_{5+x}BaLa_2Ta_2O_{11.5+0.5x}$ (x = 0−2). *Appl. Phys. A: Mater. Sci. Process.* **2008**, *91*, 615−620.

(25) Thangadurai, V.; Weppner, W. Investigations on Electrical Conductivity and Chemical Compatibility between Fast Lithium Ion Conducting Garnet-like $Li_6BaLa_2Ta_2O_{12}$ and Lithium Battery Cathodes. *J. Power Sources* **2005**, *142*, 339−344.

(26) Ramzy, A.; Thangadurai, V. Tailor-made Development of Fast Li Ion Conducting Garnet-like Solid Electrolytes. *ACS Appl. Mater. Interfaces* **2010**, *2*, 385−930.

(27) Larson, A. C.; Dreele, R. B. V. *General Structure Analysis System (GSAS)*; Los Alamos National Laboratory Report LAUR 86-748 ; Los Alamos National Laboratory: Los Alamos, NM, 2004; pp 86−748.

(28) Wang, W.-G.; Wang, X.-P.; Gao, Y.-X.; Yang, J.-F.; Fang, Q.-F. Investigation on the Stability of $Li_5La_3Ta_2O_{12}$ Lithium Ionic Conductors in Humid Environment. *Front. Mater. Sci. China* **2010**, *4*, 189−192.

(29) Truong, L.; Thangadurai, V. Soft-Chemistry of Garnet-Type $Li_{5+x}Ba_xLa_{3-x}Nb_2O_{12}$ (x = 0, 0.5, 1): Reversible H^+/Li^+ Ion-Exchange Reaction and their X-ray, ^{7}Li MAS NMR, IR, and AC Impedance Spectroscopy Characterization. *Chem. Mater.* **2011**, *12*, 3970−3977.

(30) Galven, C.; Fourquet, J.-l. Instability of the Lithium Garnet $Li_7La_3Sn_2O_{12}$: Li^+/H^+ Exchange and Structural Study. *Chem. Mater.* **2011**, *23*, 1892−1900.

(31) Galven, C.; Dittmer, J.; Suard, E.; Berre, L. Instability of Lithium Garnets against Moisture. Structural Characterization and Dynamics of $Li_{7?x}H_xLa_3Sn_2O_{12}$ and $Li_{5?x}H_xLa_3Nb_2O_{12}$. *Chem. Mater.* **2012**, *24*, 3335−3345.

(32) Larraz, G.; Orera, A.; Sanjuán, M. L. Cubic Phases of Garnet-type $Li_7La_3Zr_2O_{12}$: the Role of Hydration. *J. Mater. Chem. A* **2013**, *1*, 11419−11428.

(33) Bonanos, H.; Steele, B.; Butler, E. In *Impedance Spectroscopy*, 1st ed.; MacDonald, J., Ed.; John Wiley & Sons: New York, 1987; Chapter 4, pp 191−237.

(34) Sato, H. In *Solid Electrolytes*, 1st ed.; Geller, S., Ed.; Springer Verlag: Berlin, 1977; Chapter 2, pp 3−39.

(35) Narayanan, S.; Epp, V.; Wilkening, M.; Thangadurai, V. Macroscopic and Microscopic Li^+ Transport Parameters in Cubic Garnet-type $Li_{6.5}La_{2.5}Ba_{0.5}ZrTaO_{12}$ as Probed by Impedance Spectroscopy and NMR. *RSC Adv.* **2012**, *2*, 2553−2561.

(36) Riess, I.; Braunshtein, D.; Tannhauser, D. Density and Ionic Conductivity of Sintered $(Ce0_2)_{0.82}(Gd0_{1.5})_{0.18}$. *J. Am. Ceram. Soc.* **1981**, *82*, 479−485.

(37) Gibson, G.; Dransfield, G.; Irvine, J. Sinterability of Commercial 8 mol % Yttria-stabilized Zirconia Powders and the Effect of Sintered Density on the Ionic Conductivity. *J. Mater. Sci.* **1998**, *3*, 4297−4305.